Realistic Spin Model for Multiferroic NiI_2

Xuanyi Li,[1] Changsong Xu,[1,2,*] Boyu Liu,[1] Xueyang Li,[1] L. Bellaiche,[3] and Hongjun Xiang[1,2,†]
[1]Key Laboratory of Computational Physical Sciences (Ministry of Education), Institute of Computational Physical Sciences, State Key Laboratory of Surface Physics, and Department of Physics, Fudan University, Shanghai 200433, China
[2]Shanghai Qi Zhi Institute, Shanghai 200030, China
[3]Physics Department and Institute for Nanoscience and Engineering, University of Arkansas, Fayetteville, Arkansas 72701, USA

(Received 30 December 2022; revised 11 May 2023; accepted 17 June 2023; published 20 July 2023)

A realistic first-principle-based spin Hamiltonian is constructed for the type-II multiferroic NiI_2, using a symmetry-adapted cluster expansion method. Besides single ion anisotropy and isotropic Heisenberg terms, this model further includes the Kitaev interaction and a biquadratic term, and can well reproduce striking features of the experimental helical ground state, that are, e.g., a proper screw state, canting of rotation plane, propagation direction, and period. Using this model to build a phase diagram, it is demonstrated that, (i) the in-plane propagation direction of $\langle 1\bar{1}0\rangle$ is determined by the Kitaev interaction, instead of the long-believed exchange frustrations and (ii) the canting of rotation plane is also dominantly determined by Kitaev interaction, rather than interlayer couplings. Furthermore, additional Monte Carlo simulations reveal three equivalent domains and different topological defects. Since the ferroelectricity is induced by spins in type-II multiferroics, our work also implies that Kitaev interaction is closely related to the multiferroicity of NiI_2.

DOI: 10.1103/PhysRevLett.131.036701

The materials of van der Waals type can potentially be made into two-dimensional (2D) layers, which exhibit exceptional properties, such as massless fermions [1], valleytronics [2], ferroelectricity [3], and ferromagnetism [4,5]. Recently, electromagnetic couplings were observed in few layers and monolayers of NiI_2, which makes NiI_2 the first established 2D multiferroic [6,7].

Bulk NiI_2 has been known as a van der Walls layered type-II multiferroic. It crystallizes in a rhombohedral lattice with a space group of $R\bar{3}m$ (point group D_{3d}). Each layer of NiI_2 consists of edge-sharing NiI_6 octahedra, yielding a triangular lattice of magnetic Ni^{2+} ions, as shown in Fig. 1(a). The Ni^{2+} ion exhibits an electronic configuration of $3d^8$, with fully occupied t_{2g} orbits and half-filled e_g orbits, resulting in the spin value of $S = 1$ and a local moment of 2 μ_B on each Ni^{2+}. The ground state was determined to be a proper screw (PS) state, where spins rotate in a plane that is perpendicular to the propagation direction. This proper screw is characterized by $\boldsymbol{q} \approx (0.138, 0, 1.457)$ in the bulk system [8], which indicates in-plane propagation along $\langle 1\bar{1}0\rangle$ directions with a period of $\lambda \approx 7.23\boldsymbol{a}$, and the out-of-plane propagation arises from the interlayer antiferromagnetic (AFM) alignments. As NiI_2 is insulating, such PS state breaks the inversion symmetry and induces an electric polarization along $\langle 110\rangle$ directions [8,9].

To understand the specific propagation directions of the PS of NiI_2, analytical results on $J_1 - J_2 - J_3$ model of triangular lattice indicate that (i) the $\langle 1\bar{1}0\rangle$ propagation can be stabilized by FM J_1 and AFM J_2 with $J_2/J_1 < -1/3$; while (ii) the $\langle 110\rangle$ propagation is favored by FM J_1 and AFM J_3 with $J_3/J_1 < -1/4$ [10]. However, various models extracted from density functional theory (DFT) actually predict a $\langle 110\rangle$ propagated ground state, with J_1 and J_2 both being FM [11–14], implying that the competing $J_1 - J_2$ mechanism is not suitable for NiI_2. Moreover, even though the Heisenberg model can stabilize a $\langle 1\bar{1}0\rangle$ propagation, it cannot explain why the ground state is PS [Fig. 1(b)], instead of other degenerate helical states [Figs. 1(c) and 1(d)].

Another interesting but still elusive point is the canting of the spin rotation plane. Measurements find that the normal of the rotation plane is not along the in-plane $\langle 1\bar{1}0\rangle$ propagation direction, but rather forms an angle of 55° with the out-of-plane direction of NiI_2 bulk [8]. Such canting has been believed to be natural, as the presumed PS state should have its rotation plane being perpendicular to its propagation direction and the PS state of NiI_2 does have an out-of-plane propagation component [9,15]. However, common mechanisms cannot explain such canting, as (i) single ion anisotropy (SIA) does not favor specific canting angle; (ii) the Dzyaloshinskii-Moriya interaction (DMI) is not allowed by the inversion symmetry of NiI_2 (Note that incommensurate spin patterns are too weak to generate non-negligible DMI); and (iii) interlayer Heisenberg terms are proved to have effects neither on propagation directions nor cantings [16]. On the other hand, new forms of interactions, i.e., Kitaev interaction [11,12,17] and biquadratic interactions [13], have recently been proposed to be non-negligible in NiI_2, but their effects and interplays are

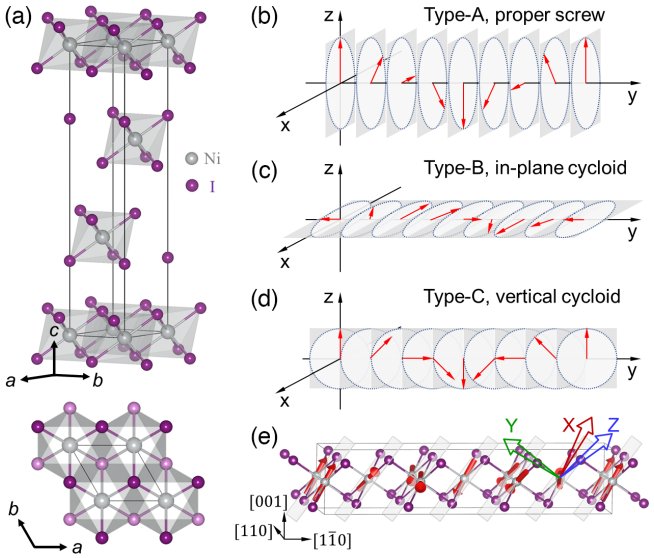

FIG. 1. Schematics of (a) NiI_2 crystal structure and common helical spin structures, (b) proper screw, (c) in-plane cycloid, and (d) vertical cycloid. Panel (e) displays the $PS^{\langle 1\bar{1}0\rangle}_{cant}$ state of NiI_2, where spins rotate in a canted plane that is spanned by the Ni_2I_2 clusters. The hollow red, green, and blue arrows denote the Kitaev basis $\{XYZ\}$.

still not clearly understood. Hence, any highly desired realistic model of NiI_2 has to not only incorporate all these aforementioned important mechanisms, but also reproduce the correct ground state—which is currently lacking.

In this Letter, we build a first-principle-based spin Hamiltonian for NiI_2, taking advantage of a symmetry-adapted cluster expansion and machine learning methods. The resulting Hamiltonian can well reproduce the observed PS state of NiI_2, with the propagation, period and canting angle comparing well with experiments on bulk systems. By further developing a phase diagram, it is demonstrated that (i) Heisenberg terms actually lead to $\langle 110\rangle$ propagation and (ii) it is the Kitaev interaction that not only results in the actual $\langle 1\bar{1}0\rangle$ propagation, but also dominantly determines the canting of the rotation plane. The roles of biquadratic interaction and interlayer couplings are also carefully examined. Monte Carlo (MC) simulations further predict diverse spin textures and topological defects.

Our newly developed symmetry-adapted cluster expansion method, as implemented in the PASP software, is applied to build the spin Hamiltonian of NiI_2 [18,19]. Such method roots in cluster expansion that goes over all combinations of spin components of $S_\alpha(\alpha = x, y, z)$. By further applying crystal symmetries to those combinations, only the symmetry-allowed terms, i.e., the invariants, are kept. The coefficients of these invariants can be fitted from total energies obtained from DFT calculations via a machine learning algorithm [20]. Such method can thus, in principle, consider all possible interactions to any body and any order [see Supplemental Material for details [21]].

TABLE I. Magnetic parameters of Eq. (1) fitted from different DFT functionals, as well as their ratio with J shown in parentheses, in units of meV. The $\perp$ symbol denotes interlayer couplings.

NiI_2	HSE		PBE	
A_{zz}	0.140	(−0.03)	0.212	(−0.05)
J	−4.976	(1.00)	−4.338	(1.00)
K	0.858	(−0.17)	1.433	(−0.33)
B	−0.719	(0.14)	−0.685	(0.16)
J_2	−0.155	(0.03)	−0.121	(0.03)
J_3	2.250	(−0.45)	3.155	(−0.73)
$J_1^\perp$	−0.048	(0.01)	−0.060	(0.01)
$J_2^\perp$	0.685	(−0.14)	1.103	(−0.25)
$J_3^\perp$	0.105	(−0.02)	0.195	(−0.04)

To construct the spin Hamiltonian of NiI_2, we start with distant neighbors going up to fifth nearest neighbors, spin-orbit coupling (SOC) effects, and up to four-body interactions (see Supplemental Material [21]). Energies of random spin structures are calculated with HSE06 hybrid functional [22], but also with PBE + U for comparison [23]. After repeated fitting and refining, the model finally reads

$$\mathcal{H} = \sum_{\langle i,j\rangle_1} \{J\mathbf{S}_i \cdot \mathbf{S}_j + K S_i^\gamma S_j^\gamma + B(\mathbf{S}_i \cdot \mathbf{S}_j)^2\} + \sum_{\langle i,j\rangle_n} J_n \mathbf{S}_i \cdot \mathbf{S}_j + \sum_{\langle i,j\rangle_n^\perp} J_n^\perp \mathbf{S}_i \cdot \mathbf{S}_j + \sum_i A_{zz} S_i^z S_i^z, \quad (1)$$

with $n = 1, 2, 3$ and where $\langle i, j\rangle_n$ denotes pairs of nth nearest neighbors (NN) within each layer, while the $\perp$ symbol refers to interlayer couplings; γ chooses its value from X, Y, and Z from the Kitaev basis [see Fig. 1(e) and Supplemental Material [21]], which shows the bond-dependent feature. Note that the SOC effects are reflected by the Kitaev term and SIA. For the sum running over $\langle i, j\rangle_1$, J quantifies the isotropic exchange coupling, K the Kitaev interaction, and B a biquadratic term. Note that one can also define $J_1 = \frac{1}{3}(3J + K)$, which can be thought of as the real isotropic exchange. A_{zz} denotes the SIA. As shown in Table I, the 1NN isotropic exchange favors FM since $J = -4.976$ meV, which is the largest coefficient in magnitude. J_2 also favors FM because of its negative sign, but is relatively very small. On the other hand, $J_3 = 2.250$ meV favors AFM and thus competes with the 1NN J. Regarding the interlayer couplings, $J_1^\perp$ is FM in nature but very small in magnitude. In contrast, $J_2^\perp = 0.685$ meV favors AFM and is the strongest interlayer coupling. Moreover, sizable AFM Kitaev interaction $K = 0.858$ and biquadratic interaction $B = -0.719$ meV are predicted, which are in line with previous studies [11–13,17,30,31]. Such spin Hamiltonian of Eq. (1) yields a very small mean averaged error (MAE) of 0.063 meV/Ni, as indicated in the Supplemental Material [21].

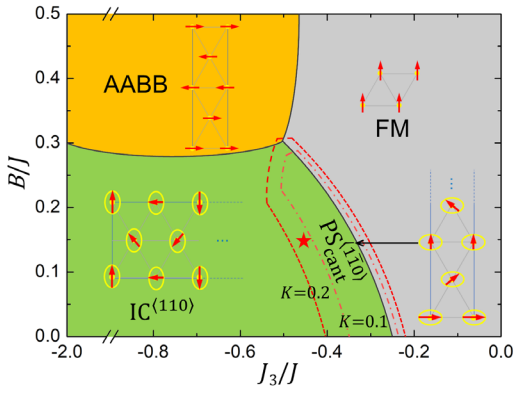

FIG. 2. Phase diagram for the studied triangular lattice. $J = -1$ meV is fixed in these calculations, J_3 and B can vary in magnitude but not in sign. The red dashed (respectively, dot-dashed) line indicates that the ground state becomes $\mathrm{IC}^{\langle 1\bar{1}0\rangle}$ (more precisely, $\mathrm{PS}^{\langle 1\bar{1}0\rangle}_{\mathrm{cant}}$) when $K/J = -0.2$ (respectively, $K/J = -0.1$). The red star denotes the model-predicted position in this phase diagram for NiI_2. Note that this phase diagram is determined by initial MC simulations and further CG optimizations, which guarantee its accuracy (see Supplemental Material for details [21]).

The ground state of NiI_2 is determined employing the Hamiltonian of Eq. (1) within MC and conjugate gradient (CG) methods. The predicted ground state indeed yields a canted PS state with an in-plane $\langle 1\bar{1}0\rangle$ propagation and antiparallel interlayer alignments, which agree well with measurements. The period is determined to be $\lambda = 7.3\boldsymbol{a}$ if neglecting interlayer couplings, which compares well with the experimental value of $\lambda = 7.23\boldsymbol{a}$ (where $\boldsymbol{a}$ denotes the in-plane lattice constant) [8,9]. Strikingly the canting angle of the rotation plane is numerically found to be 46° for bulk, which is consistent with the corresponding measured value of $55° \pm 10°$ [8]. Our model therefore reproduces well the correct PS state for bulk, where the spin texture in a single layer will be referred to as $\mathrm{PS}^{\langle 1\bar{1}0\rangle}_{\mathrm{cant}}$ state. Note that the parameters from PBE result in the $\langle 110\rangle$ propagation, as a result of rather strong J_3/J. It is also important to know that isotropic Heisenberg terms, by themselves, do not support in-plane $\langle 1\bar{1}0\rangle$ propagation, as J_2 and J both favor FM while J_3 and J compete against each other (since $J_3 > 0$ and thus favor AFM while $J_3/J = -0.45$). Such isotropic Heisenberg terms lead to an incommensurate state along $\langle 110\rangle$ ($\mathrm{IC}^{\langle 110\rangle}$), which is consistent with both analytical results [10] and previous models from DFT [11–14]. It therefore indicates that the $\langle 1\bar{1}0\rangle$ propagation is stabilized by mechanisms other than the isotropic Heisenberg terms.

To unravel the puzzling mechanisms that stabilize such $\langle 1\bar{1}0\rangle$ propagation, we built a phase diagram. More precisely, we chose $J = -1$ meV and sweep over $J_3 \geq 0$ and $B \leq 0$ (in this phase diagram, "only" J, J_3, and B are thus included for now). As shown in Fig. 2, for $B/J = 0$, the chosen negative J stabilizes the FM state when J_3 is weak; while the system adopts $\mathrm{IC}^{\langle 110\rangle}$ states when $J_3/J < -0.25$, which is consistent with the analytical results of Ref. [10]. For $B/J > 0$, the negative biquadratic term shifts the $\mathrm{IC}^{\langle 110\rangle}$-FM boundary toward larger magnitude of J_3/J, which can be understood by the fact that $B < 0$ favors collinear arrangements and thus helps stabilize the FM state. When $B/J \gtrsim 0.3$ and $J_3/J \lesssim -0.5$, a so-called AABB AFM state becomes the ground state [32]. Moreover, calculations varying the interlayer Heisenberg terms ($J_n^{\perp}$, $n = 1, 2, 3$) were also performed, but their results are not shown in the phase diagram. It is found that $J_n^{\perp}$ can only modify the period of IC states or induce collinear states, but not alter the propagation direction, which is in line with a previous work too [16]. The phase diagram discussed so far thus indicates that J, J_3, B, and $J_n^{\perp}$, by themselves, cannot lead to the $\langle 1\bar{1}0\rangle$ propagation in the investigated parameter space.

The Kitaev interaction is therefore now further incorporated into the computations and resulting phase diagram (consequently, J, J_3, B, and K are now included in this new phase diagram). Surprisingly, with $K = 0.1$ meV (resulting thus in $K/J = -0.1$), an incommensurate state propagating along $\langle 1\bar{1}0\rangle$ ($\mathrm{IC}^{\langle 1\bar{1}0\rangle}$) emerges at the border of the previous $\mathrm{IC}^{\langle 110\rangle}$-FM transition, as additionally shown in Fig. 2. Such $\mathrm{IC}^{\langle 1\bar{1}0\rangle}$ state takes a slim area of the previous FM zone and a relatively large area of the previous $\mathrm{IC}^{\langle 110\rangle}$ state. When increasing the Kitaev interaction even more to $K = 0.2$ meV, the area of $\mathrm{IC}^{\langle 1\bar{1}0\rangle}$ state further expands. As a result, the phase points defined by, e.g., $J_3/J = -0.4$ and $B/J = 0$, as well as $J_3/J = -0.5$ and $B/J = 0.2$, transform from the $\mathrm{IC}^{\langle 110\rangle}$ to $\mathrm{IC}^{\langle 1\bar{1}0\rangle}$ state. It is thus clear that, for NiI_2, the ratios $J_3/J = -0.45$ and $B/J = 0.14$ favor the $\mathrm{IC}^{\langle 110\rangle}$ state, but $K/J = -0.17$ renders the ground state to become the $\mathrm{IC}^{\langle 1\bar{1}0\rangle}$ state. Such results therefore demonstrate that the Kitaev interaction (with $K > 0$), along with the frustration between J and J_3, tends to stabilize the $\langle 1\bar{1}0\rangle$ propagation.

Moreover, it is found that the aforementioned $\mathrm{IC}^{\langle 1\bar{1}0\rangle}$ state resulted from the J-K-J_3(-B) model (i.e., a model with only such terms) also exhibits canted rotation plane. This canting angle between the Y axis and out-of-plane direction yields 54.7°, implying that the canting plane locates exactly in the XZ plane [see Fig. 1(e) for the Kitaev basis]. If we focus on a single layer, such canted $\mathrm{IC}^{\langle 1\bar{1}0\rangle}$ state is actually the $\mathrm{PS}^{\langle 1\bar{1}0\rangle}_{\mathrm{cant}}$ state of NiI_2. Such fact strongly suggests that the canting of the $\mathrm{PS}^{\langle 1\bar{1}0\rangle}_{\mathrm{cant}}$ state for NiI_2 is strongly related to the Kitaev interaction. To verify such point, we turned on only the intralayer terms of Eq. (1) and compare the energies of three phases: (i) $\mathrm{PS}^{\langle 1\bar{1}0\rangle}_{\mathrm{cant}}$ state with a period of $\lambda = 7.25\boldsymbol{a}$; (ii) artificially made $\mathrm{PS}^{\langle 1\bar{1}0\rangle}$ state (that has no canting) with $\lambda = 7.25\boldsymbol{a}$; and (iii) artificially made $\mathrm{PS}^{\langle 110\rangle}$ state (that has also no canting) with $\lambda = 6.25\boldsymbol{a}$. Note that the chosen

TABLE II. Total energy and relative energies of different PS states, as well as the decomposition of these energies into specific interaction, as calculated with the HSE parameters in Table I (unit: meV/Ni). Para. represents Parameters.

Para.	$PS^{\langle 1\bar{1}0\rangle}_{cant}$	$PS^{\langle 1\bar{1}0\rangle}$	$PS^{\langle 110\rangle}$	$PS^{\langle 1\bar{1}0\rangle}$ -$PS^{\langle 110\rangle}$	$PS^{\langle 1\bar{1}0\rangle}_{cant}$ -$PS^{\langle 110\rangle}$	$PS^{\langle 1\bar{1}0\rangle}_{cant}$ -$PS^{\langle 1\bar{1}0\rangle}$
A_{zz}	0.04	0.07	0.07	0.00	−0.03	−0.03
J	−11.42	−11.42	−11.39	−0.03	−0.03	0.00
K	0.56	0.61	0.61	0.00	−0.05	−0.05
B	0.84	0.84	0.85	−0.01	−0.01	−0.00
J_2	−0.18	−0.18	−0.17	−0.00	−0.00	0.00
J_3	1.52	1.52	1.45	0.07	0.07	0.00
Total	−8.64	−8.56	−8.59	0.03	−0.05	−0.08

periods lead to the lowest energy of the corresponding propagation. The total and decomposed energies of the three phases are listed in Table II. It is found that, (a) $PS^{\langle 1\bar{1}0\rangle}$ is 0.03 meV/Ni higher in energy than $PS^{\langle 110\rangle}$ and the Kitaev term contributes the same energy to both states, indicating that the Kitaev interaction favors $PS^{\langle 1\bar{1}0\rangle}$ and $PS^{\langle 110\rangle}$ equally; while (b) $PS^{\langle 1\bar{1}0\rangle}_{cant}$ is 0.08 meV/Ni lower in energy than $PS^{\langle 1\bar{1}0\rangle}$, and the Kitaev interaction, as well as the SIA, contributes dominantly to this energy gain. Such comparisons thus demonstrate that the Kitaev interaction favors canting altogether with the $\langle 1\bar{1}0\rangle$ propagation. Moreover, it indicates that Kitaev interaction favors spins rotating in ZX, XY, or YZ planes with a canting angle of 54.7°, while the in-plane SIA further pushes the rotation plane toward the basal plane with a canting angle of 46°.

We then develop a model to better understand why Kitaev interaction favors $\langle 1\bar{1}0\rangle$ propagation, as well as, a canting in rotation plane (see details in Supplemental Material [21]). Here, we construct $PS^{\langle 1\bar{1}0\rangle}$ and $PS^{\langle 110\rangle}$ states and adopt only the Kitaev interaction. The resulted energies are expressed as $E^{1\bar{1}0}/K = c_1(\cos 2\theta_1 - 2\sqrt{2}\sin 2\theta_1) + c_2$ and $E^{110}/K = c_3 \cos 2\theta_1 + c_4$, where $E^{1\bar{1}0}$ and E^{110} are the total energies of the corresponding PS states, θ_1 is the angle from the [001] direction to the normal of the rotation plane, and $c_n (n = 1\text{–}4)$ are positive constants. It is found that (i) $E^{1\bar{1}0}$ has its minimum at $\theta_1 = 54.7°$, which is the angle between the [001] direction and the Y (Z or X, respectively) axis, demonstrating that the Kitaev interaction prefers the rotation plane of the $PS^{\langle 1\bar{1}0\rangle}$ pattern within the XZ (XY or YZ, respectively) plane; (ii) E^{110} has its minimum at $\theta_1 = \pm 90°$, indicating an exact PS state with the rotation plane being perpendicular to the propagation direction; and (iii) $E^{1\bar{1}0}_{min} < E^{110}_{min}$, confirming that $\langle 1\bar{1}0\rangle$ propagation, together with a canting, is energetically more favorable (see Fig. S3 of Supplemental Material [21]).

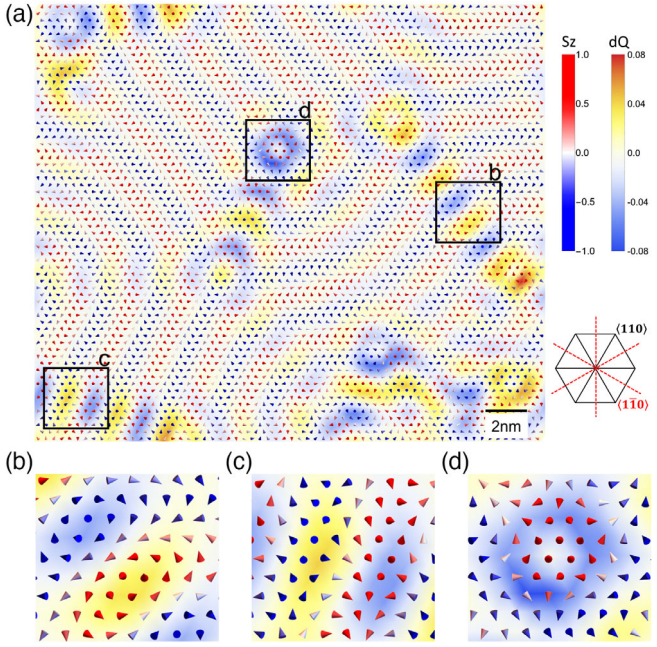

FIG. 3. Panel (a) displays spin patterns of NiI_2 from MC simulation and a following CG optimization [34]. Panels (b),(c) and (d), respectively, show an enlarged view of the topological defects occurring in panel (a). Spins are represented by cones, with the red and blue colors showing positive and negative values of the S_z component. For all these panels, the colors used for the background quantify the topological charges, dQ.

The critical role of Kitaev interaction in reproducing the canting in the spin rotation plane demonstrates the significance of SOC effects on the spin model of NiI_2. Moreover, our DFT results (see Fig. S7 of Supplemental Material) show that the strength of electric polarization depends largely on the orientation of the spin rotation plane. It thus indicates that the Kitaev interaction is closely related to the ferroelectricity. Such findings are thus in line with previous work, which demonstrates that the ferroelectric order is controlled by the SOC of iodine [33].

Furthermore, Monte Carlo simulations, as well as a conjugate gradient (CG) algorithm, are performed on large supercells using the Hamiltonian of Eq. (1). Since bulk only differs from the monolayer only by a longer period of propagation and interlayer AFM alignments, we focus on the monolayer hereafter for simplicity. As shown in Fig. 3(a), these simulations found that canted PS states form stripy domains and cover most of the area at low temperatures, which is consistent with the fact that the $PS^{\langle 1\bar{1}0\rangle}_{cant}$ states are the ground states of NiI_2 bulk. There are three domains that propagate along $\langle 1\bar{1}0\rangle$ or the equivalent $\langle 120\rangle$ and $\langle \bar{2}\,\bar{1}\,0\rangle$ directions, which is also in line with the observed three domains of NiI_2 monolayer [7]. Note that the spin pattern shown in Fig. 3(a) is only 0.038 meV/Ni higher in energy than the ground state of $PS^{\langle 1\bar{1}0\rangle}_{cant}$ monodomain. Interestingly, topological defects are predicted to

occur at phase boundaries (see Fig. 3), which is in line with the prediction of skyrmion lattice in monolayer NiI_2 [11].

To conclude, we adopted the symmetry-adapted cluster expansion method and built a realistic spin model for multiferroic NiI_2. Such a model can reproduce well the experimental $\langle 1\bar{1}0\rangle$ propagating proper screw state, as well as the canting in its spin rotation plane. The Kitaev interaction is found to play a key role in NiI_2 and is proved to impose anisotropy on coplanar spin texture. Our work thus leads to a better understanding on the magnetism of NiI_2, as well as its type-II multiferroicity.

We acknowledge financial support from the National Key R&D Program of China (No. 2022YFA1402901), NSFC (Grants No. 11825403, No. 11991061, No. 12188101, No. 12174060, and No. 12274082), the Guangdong Major Project of the Basic and Applied basic Research (Future functional materials under extreme conditions–2021B0301030005), and Shanghai Pilot Program for Basic Research—FuDan University 21TQ1400100 (23TQ017). C. X. also acknowledges support from the Shanghai Science and Technology Committee (Grant No. 23ZR1406600) and the open project of Guangdong provincial key laboratory of magnetoelectric physics and devices (No. 2020B1212060030). L. B. acknowledges support from the Vannevar Bush Faculty Fellowship (VBFF) from the Department of Defense, the ARO Grant No. W911NF- 352-21-2-0162 (ETHOS) and Award No. DMR-1906383 from the National Science Foundation Q-AMASE-i Program (MonArk NSF Quantum Foundry). The Arkansas High Performance Computing Center (AHPCC) is also acknowledged.

*csxu@fudan.edu.cn
†hxiang@fudan.edu.cn

[1] Kostya S. Novoselov, Andre K. Geim, Sergei Vladimirovich Morozov, Dingde Jiang, Michail I. Katsnelson, L. V. Grigorieva, S. V. Dubonos, and A. A. Firsov, Two-dimensional gas of massless Dirac fermions in graphene, Nature (London) **438**, 197 (2005).

[2] Kin Fai Mak, Keliang He, Jie Shan, and Tony F. Heinz, Control of valley polarization in monolayer MoS_2 by optical helicity, Nat. Nanotechnol. **7**, 494 (2012).

[3] Kai Chang, Junwei Liu, Haicheng Lin, Na Wang, Kun Zhao, Anmin Zhang, Feng Jin, Yong Zhong, Xiaopeng Hu, Wenhui Duan *et al.*, Discovery of robust in-plane ferroelectricity in atomic-thick SnTe, Science **353**, 274 (2016).

[4] Cheng Gong, Lin Li, Zhenglu Li, Huiwen Ji, Alex Stern, Yang Xia, Ting Cao, Wei Bao, Chenzhe Wang, Yuan Wang *et al.*, Discovery of intrinsic ferromagnetism in two-dimensional van der Waals crystals, Nature (London) **546**, 265 (2017).

[5] Bevin Huang, Genevieve Clark, Efren Navarro-Moratalla, Dahlia R. Klein, Ran Cheng, Kyle L. Seyler, Ding Zhong, Emma Schmidgall, Michael A. McGuire, David H. Cobden *et al.*, Layer-dependent ferromagnetism in a van der Waals crystal down to the monolayer limit, Nature (London) **546**, 270 (2017).

[6] Hwiin Ju, Youjin Lee, Kwang-Tak Kim, In Hyeok Choi, Chang Jae Roh, Suhan Son, Pyeongjae Park, Jae Ha Kim, Taek Sun Jung, Jae Hoon Kim *et al.*, Possible persistence of multiferroic order down to bilayer limit of van der Waals material NiI_2, Nano Lett. **21**, 5126 (2021).

[7] Qian Song, Connor A. Occhialini, Emre Ergeçen, Batyr Ilyas, Danila Amoroso, Paolo Barone, Jesse Kapeghian, Kenji Watanabe, Takashi Taniguchi, Antia S. Botana *et al.*, Evidence for a single-layer van der Waals multiferroic, Nature (London) **602**, 601 (2022).

[8] S. R. Kuindersma, J. P. Sanchez, and C. Haas, Magnetic and structural investigations on NiI_2 and CoI_2, Physica (Amsterdam) **111B+C**, 231 (1981).

[9] T. Kurumaji, S. Seki, S. Ishiwata, H. Murakawa, Y. Kaneko, and Y. Tokura, Magnetoelectric responses induced by domain rearrangement and spin structural change in triangular-lattice helimagnets NiI_2 and CoI_2, Phys. Rev. B **87**, 014429 (2013).

[10] Tsuyoshi Okubo, Sungki Chung, and Hikaru Kawamura, Multiple-q States and the Skyrmion Lattice of the Triangular-Lattice Heisenberg Antiferromagnet under Magnetic Fields, Phys. Rev. Lett. **108**, 017206 (2012).

[11] Danila Amoroso, Paolo Barone, and Silvia Picozzi, Spontaneous skyrmionic lattice from anisotropic symmetric exchange in a Ni-halide monolayer, Nat. Commun. **11**, 5784 (2020).

[12] K. Riedl, D. Amoroso, S. Backes, A. Razpopov, Thi Phuong Thao Nguyen, K. Yamauchi, P. Barone, S. M. Winter, S. Picozzi, and R. Valentí, Microscopic origin of magnetism in monolayer 3d transition metal dihalides, Phys. Rev. B **106**, 035156 (2022).

[13] J. Y. Ni, X. Y. Li, D. Amoroso, X. He, J. S. Feng, E. J. Kan, S. Picozzi, and H. J. Xiang, Giant Biquadratic Exchange in 2d Magnets and its Role in Stabilizing Ferromagnetism of $NiCl_2$ Monolayers, Phys. Rev. Lett. **127**, 247204 (2021).

[14] Xiao-sheng Ni, Dao-Xin Yao, and Kun Cao, In-plane strain tuning multiferroicity in monolayer van der Waals NiI_2, arXiv:2209.12392.

[15] T. Kurumaji, S. Seki, S. Ishiwata, H. Murakawa, Y. Tokunaga, Y. Kaneko, and Y. Tokura, Magnetic-Field Induced Competition of Two Multiferroic Orders in a Triangular-Lattice Helimagnet MnI_2, Phys. Rev. Lett. **106**, 167206 (2011).

[16] L. P. Régnault, J. Rossat-Mignod, A. Adam, D. Billerey, and C. Terrier, Inelastic neutron scattering investigation of the magnetic excitations in the helimagnetic state of $NiBr_2$, J. Phys. France **43**, 1283 (1982).

[17] P. Peter Stavropoulos, D. Pereira, and Hae-Young Kee, Microscopic Mechanism for a Higher-Spin Kitaev Model, Phys. Rev. Lett. **123**, 037203 (2019).

[18] Feng Lou, X. Y. Li, J. Y. Ji, HY Yu, J. S. Feng, X. G. Gong, and H. J. Xiang, PASP: Property analysis and simulation package for materials, J. Chem. Phys. **154**, 114103 (2021).

[19] Changsong Xu, Xueyang Li, Peng Chen, Yun Zhang, Hongjun Xiang, and Laurent Bellaiche, Assembling diverse skyrmionic phases in Fe_3GeTe_2 monolayers, Adv. Mater. **34**, 2107779 (2022).

[20] Xue-Yang Li, Feng Lou, Xin-Gao Gong, and Hongjun Xiang, Constructing realistic effective spin Hamiltonians with machine learning approaches, New J. Phys. **22**, 053036 (2020).

[21] See Supplemental Material at http://link.aps.org/supplemental/10.1103/PhysRevLett.131.036701 for detailed methods and further discussions, which includes Refs. [8,11,13,16,18,20,22–29].

[22] Aliaksandr V. Krukau, Oleg A. Vydrov, Artur F. Izmaylov, and Gustavo E. Scuseria, Influence of the exchange screening parameter on the performance of screened hybrid functionals, J. Chem. Phys. **125**, 224106 (2006).

[23] John P. Perdew, Kieron Burke, and Matthias Ernzerhof, Generalized Gradient Approximation Made Simple, Phys. Rev. Lett. **77**, 3865 (1996).

[24] Georg Kresse and Jürgen Furthmüller, Efficient iterative schemes for *ab initio* total-energy calculations using a plane-wave basis set, Phys. Rev. B **54**, 11169 (1996).

[25] P. E. Blöchl, Projector augmented-wave method, Phys. Rev. B **50**, 17953 (1994).

[26] Magnus Rudolph Hestenes and Eduard Stiefel, *Methods of Conjugate Gradients for Solving Linear Systems* (National Bureau of Standards Washington, DC, 1952), Vol. 49.

[27] Changsong Xu, Junsheng Feng, Sergei Prokhorenko, Yousra Nahas, Hongjun Xiang, and Laurent Bellaiche, Topological spin texture in Janus monolayers of the chromium trihalides $Cr(I,X)_3$, Phys. Rev. B **101**, 060404(R) (2020).

[28] Minsoo Kim, Piranavan Kumaravadivel, John Birkbeck, Wenjun Kuang, Shuigang G. Xu, D. G. Hopkinson, Johannes Knolle, Paul A. McClarty, A. I. Berdyugin, M. Ben Shalom *et al.*, Micromagnetometry of two-dimensional ferromagnets, Nature Electronics **2**, 457 (2019).

[29] Zefang Li, Dong-Hong Xu, Xue Li, Hai-Jun Liao, Xuekui Xi, Yi-Cong Yu, and Wenhong Wang, Anomalous spin dynamics in a two-dimensional magnet induced by anisotropic critical fluctuations, Phys. Rev. B **106**, 054427 (2022).

[30] Changsong Xu, Junsheng Feng, Hongjun Xiang, and Laurent Bellaiche, Interplay between Kitaev interaction and single ion anisotropy in ferromagnetic CrI_3 and $CrGeTe_3$ monolayers, npj Comput. Mater. **4**, 57 (2018).

[31] Changsong Xu, Junsheng Feng, Mitsuaki Kawamura, Youhei Yamaji, Yousra Nahas, Sergei Prokhorenko, Yang Qi, Hongjun Xiang, and L. Bellaiche, Possible Kitaev Quantum Spin Liquid State in 2D Materials with $S = 3/2$, Phys. Rev. Lett. **124**, 087205 (2020).

[32] Linlu Wu, Linwei Zhou, Xieyu Zhou, Cong Wang, and Wei Ji, In-plane epitaxy-strain-tuning intralayer and interlayer magnetic coupling in $CrSe_2$ and $CrTe_2$ monolayers and bilayers, Phys. Rev. B **106**, L081401 (2022).

[33] Adolfo O. Fumega and J. L. Lado, Microscopic origin of multiferroic order in monolayer NiI_2, 2D Mater. **9**, 025010 (2022).

[34] Note that the spin patterns in Fig. 3(a) do not correspond to a MC temperature, as the CG algorithm leads the pattern to a stable state, which is a global or local energy minimum.